Journal of Materials Chemistry A

Maximizing Active Site Utilization in Carbocatalysts for High-Performance Oxygen Reduction Reactions and Zinc-Air Battery-Powered Capacitive Deionization

Journal:	*Journal of Materials Chemistry A*
Manuscript ID	TA-COM-05-2024-003422.R1
Article Type:	Communication
Date Submitted by the Author:	07-Jul-2024
Complete List of Authors:	Mou, Xiaofeng; Hebei Agricultural University Zhang, Jiale; Hebei Agricultural University Zhao, Bin; Hebei Agricultural University Dong, Yanli; Hebei Agricultural University Liu, Huimin; Hebei Agricultural University, Department of Chemistry, College of Science Liang, Jiaxu; Max Planck Institute for Polymer Research, Xin, Xiaoyu; Hebei Agricultural University Asakura, Yusuke; Nagoya Daigaku, Graduate School of Engineering Zhang, Shuaihua; Hebei Agricultural University, College of Science Xiao, Zhichang; Hebei Agricultural University, Department of Chemistry, College of Science Yamauchi, Yusuke; University of Queensland, Chemical Engineering; Nagoya University,

Maximizing Active Site Utilization in Carbocatalysts for High-Performance Oxygen Reduction Reactions and Zinc-Air Battery-Powered Capacitive Deionization

Xiaofeng Mou[1], Jiale Zhang[1], Bin Zhao[1], Yanli Dong[1], Huimin Liu[1], Jiaxu Liang[2]*, Xiaoyu Xin[1], Yusuke Asakura[3], Shuaihua Zhang[1]*, Zhichang Xiao[1]* and Yusuke Yamauchi[3, 4, 5]*

[1] Department of Chemistry, College of Science, Hebei Agricultural University, Baoding 071001, People's Republic of China.

[2] Max Planck Institute for Polymer Research, Ackermannweg 10, 55128 Mainz, Germany

[3] Department of Materials Process Engineering, Graduate School of Engineering, Nagoya University, Nagoya 464-8603, Japan

[4] Australian Institute for Bioengineering and Nanotechnology (AIBN), The University of Queensland, Brisbane, QLD 4072, Australia

5 Department of Chemical and Biomolecular Engineering, Yonsei University, 50 Yonsei-ro, Seodaemun-gu, Seoul 03722, South Korea

*Corresponding authors:

E-mail: liangjiaxu@mpip-mainz.mpg.de (J. Liang); zhangshuaihua@hebau.edu.cn (S. Zhang); xiaozhichangcnu@sina.cn (Z. Xiao); y.yamauchi@uq.edu.au (Y. Yamauchi).

Abstract: The underutilization of active sites limits the performance enhancement of functional carbon nanomaterials in electrocatalytic oxygen reduction reactions (ORR). Here, we propose a molten salt-regulated synthesis of indole-based hypercrosslinked polymers to create a series of nitrogen-doped porous carbon materials (NPC) with controllable quantities of active sites and specific surface areas (SSA). A deep investigation of the structure-property relationship indicates that the environment of the active sites, particularly the electrochemical active surface area (ECSA), plays a pivotal supporting role. Furthermore, the ECSA per active site (EPA) correlates directly with ORR performance. The NPC-Zn catalyst, which possesses the highest EPA, demonstrates the highest half-wave potential (0.859 V) and kinetic current density (102.64 mA cm^{-2}), and excellent performance in the rechargeable zinc-air battery (ZAB). Furthermore, the NPC-Zn-based capacitive deionization (CDI) device, powered by NPC-Zn-based ZAB, exhibits a stable adsorption capacity of 27.8 mg g^{-1} for 6 hours, which is consistent with that driven by a direct-current supply. This work provides new insights into the utilization efficiency of active sites in carbocatalysts for ORR, serving as a prime example for designing high-performance ORR electrocatalysts with broad application prospects in the field of environmental energy.

Keywords: oxygen reduction reaction; microenvironment; utilization of active sites; zinc-air batteries; self-powered capacitive deionization

1. Introduction

Zinc-air batteries (ZABs) have become increasingly prominent in the field of energy and environmental sustainability, attributed to their high energy density and environmental compatibility.[1, 2] These batteries are particularly attractive for their potential in both grid-scale storage and portable applications. However, the widespread adoption of ZABs is still hampered by the slow kinetics of the oxygen reduction reaction (ORR) at the cathode.[3, 4] Up to now, platinum-based materials are the most effective catalysts for facilitating ORR. However, their high cost and scarcity limit their practicality for widespread, cost-effective implementation in ZABs.[5]

Metal-free defective carbon materials have garnered tremendous attention for their chemical stability, high catalytic activity, and low cost.[6] Defect structures within these carbon materials, such as heteroatom doping and intrinsic carbon defects, are recognized to be crucial for enhancing ORR performance.[7, 8] Among the heteroatom dopants in carbon materials, nitrogen has received significant attention for its ability to alter the electronic properties of adjacent carbon atoms, facilitating oxygen adsorption and reduction.[9] Although there is debate over which type of nitrogen plays the predominant role in nitrogen-doped carbocatalysts, theoretical calculations and experimental verifications recognize that pyridinic and graphitic nitrogen are the main active sites.[10-12] Therefore, researchers are diligently exploring material preparation methods to increase the quantity of nitrogen dopant, with the aim of enhancing the ORR performance of these materials. For instance, Wu et al. synthesized pyridinic nitrogen-dominated nitrogen-doped graphene through a CVD growth process, which contained

a high nitrogen content of 6.5 at% and an onset potential of 0.97 V vs. RHE in ORR process.[13] Yu et al. developed a novel strategy using g-C_3N_4 as the template, porogen, and nitrogen source, resulting in the N-CNS-120 catalyst with a high nitrogen content of 11.6 at% and an impressively high $E_{1/2}$ of -0.210 V (vs. Ag/AgCl).[14]

On the other hand, the presence of various defect types such as pentagon,[15, 16] heptagon,[17] vacancy,[18] and edge defects[19] within the carbon frameworks could regulate their electronic distribution, which have been confirmed to function as active sites in ORR process. To increase the ORR activity of the metal-free defective carbocatalysts, Wu et al. constructed ultra-dense carbon defects (2.46×10^{13} cm^{-2}) in the carbocatalyst, which showed a superior half-wave potentials of 0.90 V compared to 0.81 V of the carbocatalyst with a lower defect density (3.01×10^{12} cm^{-2}) porous carbon.[20] While the focus has commonly been on increasing the number of active sites in metal-free defective carbocatalysts to enhance ORR performance, recent insights suggest that the microenvironment of these active sites plays an equally critical role.[21-23] Thus, optimizing the microenvironment of active sites in metal-free defective carbon catalysts is a research field of great interest. As a very hot research field, highly dispersed metal sites in both precious and non-precious metal carbon catalysts can form atomic-level dispersed structures, enabling the most efficient utilization of active sites. [24, 25] Inspired by this, we hypothesize that controlling the microenvironment of active sites in non-metal defective carbon catalysts, thereby achieving high dispersion of these sites, could enhance their effective utilization and improve ORR performance.

Direct pyrolysis of porous organic polymers (POPs) represents a promising approach

for synthesizing high-performance carbocatalysts due to the diverse synthetic strategies available from designated building blocks.[26, 27] However, the dilemma of pore collapse during thermal crosslinking process often results in a low retention rate of the pore structure, decreased surface area and inferior accessibility of active sites.[28] Molten salt-assisted treatment offers a great opportunity to tackle this problem by preserving the pore structure. Meanwhile, abundant defect structures and heteroatom dopants can be introduced into the derived carbonaceous network, thus facilitating the efficient utilization of active sites in defective carbocatalysts.[29, 30] Yet, reports on using affordable molten salt treatment to control the microenvironment, particularly to aid maximizing the utilization efficiency of active sites in POPs for enhanced ORR performance, are still scarce.

Herein, we present a method using molten salt-assisted pyrolysis of indole-based POPs to produce nitrogen-doped porous carbon (NPC) materials, achieving high efficiency in nitrogen dopant/defect structure utilization. Interestingly, the use of different types of molten salt treatment on NPC can change the efficiency of nitrogen doping/defect structure utilization. Among the different molten salt-treated NPC, the NPC treated with zinc chloride (NPC-Zn) exhibits the highest electrochemical active surface area (ECSA) per nitrogen atom and defect structure. This high ECSA per active site (EPA) guarantees maximal utilization of active sites during electrocatalytic ORR, exhibiting a $E_{1/2}$ of 0.859 V vs. RHE and a kinetic current density of 102.64 mA cm^{-2}. The ZAB assembled with this NPC-Zn catalyst exhibits excellent stability and ultra-high energy density. The high SSA and abundant nitrogen content also endow NPC-Zn

with outstanding capacitive desalination ability in CDI. Impressively, the ZAB assembled with NPC-Zn provides a stable output voltage of 1.443 V, and drives an NPC-Zn-based CDI device to maintain its capacitive desalination capacity of up to 27.8 mg g^{-1} even after 6 hours of continuous operation, demonstrating the significant advantages of this catalyst with high EPA characteristics in practical electrocatalytic ORR applications.

2. Experimental section

Preparation of indole-HCP: 1.6 g of anhydrous ferric chloride was placed into a pressure flask. Then, 10 mL of dichloroethane and 2700 μL of dimethoxymethane (Dimethoxymethane is an acetal that is the dimethyl acetal derivative of formaldehyde, FDA) were added, followed by stirring in an ice bath for 10 minutes. Then, 1.1715 g (0.01 mol) of indole, which was pre-dissolved in 10 mL of dichloroethane, was slowly added *via* a dropping funnel. The obtained mixture was continuously stirred in an ice bath for 20 minutes. Then, the mixture was first heated in oil bath at 45 ℃ for 5 hours, and then heated at 80 ℃ for 19 hours. After cooling to room temperature, the mixture was filtered and extracted with 2 M hydrochloric acid solution for 24 hours. The obtained brown product was dried overnight in an oven at 80 ℃, and was named as indole-based hypercrosslinked polymers (indole-HCP).

Preparation of NPC-Zn: 500 mg of indole-HCP precursor was dispersed in 40 ml of anhydrous ethanol. Subsequently, 2.5 g of zinc chloride was added to the above solution. The solution was sonicated for 30 minutes, and then heated in an oil bath at 80 ℃ until

the solvent was completely evaporated to yield a solid mixture. The mixture was transferred into an alumina boat and carbonized in a tube furnace under an argon atmosphere, and heated to 400 ℃ at a rate of 5 ℃/min for pre-carbonization for 3 hours, after which the temperature was increased to 800 ℃ for 1 hour. The product was thoroughly washed with hydrochloric acid solution (2 M) in a Soxhlet extractor for 24 hours, and dried overnight in an oven at 80 ℃ to obtain a black powder, which was noted as NPC-Zn.

Preparation of NPC-Fe and NPC-Na: The method was the same as that used for NPC-Zn, except that 2.5 g of zinc chloride was replaced with 2.5 g of anhydrous ferric chloride and sodium chloride, respectively.

Preparation of NC-800: Without adding any molten salt, 500 mg of the precursor was placed directly into the tube furnace. The subsequent carbonization and washing processes were carried out in the same manner as those for NPC-Zn.

3. Results and discussion

The synthesis of nitrogen-doped porous carbon (NPC) and its corresponding molten salt-treated samples is illustrated in Scheme 1. Firstly, the indole-HCP were fabricated through a typical Friedel-Crafts alkylation process,[31] during which indole molecules with FDA were cross-linked. Subsequently, the indole-HCP underwent either a direct thermal treatment or a molten salt-assisted treatment under an inert atmosphere to yield the NPC or NPC-M, where “M” represents the metal element in the salt halide, including Na, Zn, and Fe. The choice of indole as the nitrogen source in this work is primarily due to its unique bicyclic structure combining a benzene ring and a pyrrole

ring, which offers a stable yet reactive framework for hyper crosslinking and facilitates the formation of a robust porous polymer structure. The inherent nitrogen in the indole molecule is ideally positioned for efficient nitrogen doping during the carbonization process, thereby maintaining the high nitrogen content in the resultant NPC as well as NPC-M.

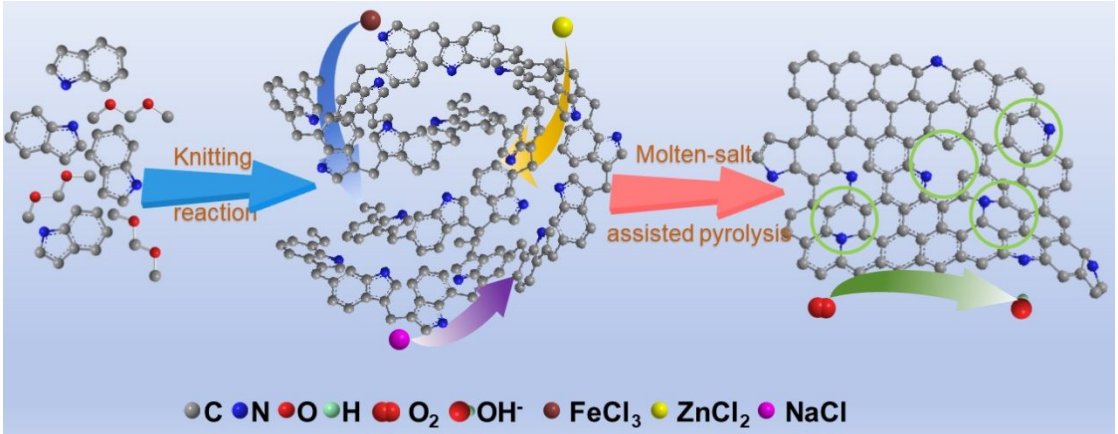

Scheme 1. Illustration for the synthesis of indole-HCP and NPC-M.

The microscopic morphology of the samples was characterized by scanning electron microscope (SEM) and transmission electron microscopy (TEM). SEM images show that the NPC sample possesses a fibrous cluster structure (Fig. 1a). The sample treated with sodium chloride (NPC-Na) exhibits a neuron-like network structure (Fig. 1b). The zinc chloride-treated sample (NPC-Zn) shows a flake-like structure (Fig. 1c), and the iron chloride-treated sample (NPC-Fe) demonstrates a dispersed fibrous structure (Fig. 1d). TEM images (Fig. 1e-h) corroborate the observations from SEM. Intriguingly, the NPC-Zn sample exhibits distinct pore structures (Fig. 1g), suggesting that the zinc chloride molten salt treatment of indole-HCP successfully creates specific pore channels within the sample. Elemental distribution analysis of the NPC-Zn sample,

using high-angle annular dark-field scanning transmission electron microscopy (HAADF-STEM) and corresponding elemental mapping (Fig. 1i), confirms the uniform distribution of nitrogen and oxygen elements within the carbon framework. This indicates that the nitrogen from the indole molecules is successfully incorporated into the NPC-Zn sample. The presence of oxygen element is probably due to partially unreacted methoxy functional groups from the crosslinking agent FDA remaining in the polymer molecular chains. Aberration-corrected TEM (Fig. S1) analysis of NPC-Zn reveals an abundance of topological defects, including pentagon, heptagon, and vacancy. In sum, the electron microscopy analysis indicates that the NPC-Zn sample indeed possesses active sites, including nitrogen heteroatoms and defect structures, which are beneficial for enhancing the electrocatalytic ORR performance.

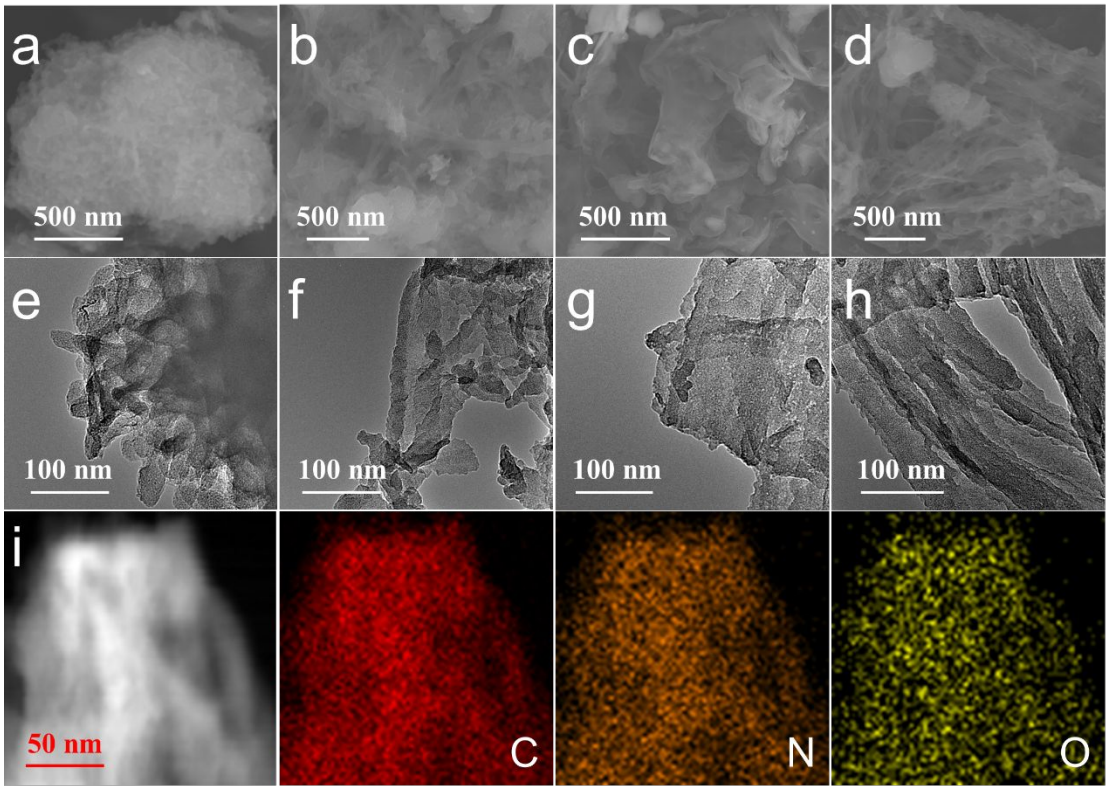

Figure 1. Microscopic morphology analysis of NPC samples. SEM images of (a) NPC, (b) NPC-Na, (c) NPC-Zn and (d) NPC-Fe; TEM images of (e) NPC, (f) NPC-Na, (g)

NPC-Zn and (h) NPC-Fe; (i) HADDF image and the corresponding elemental mapping images of NPC-Zn.

Subsequently, the defect structures of the samples are analyzed using X-ray diffraction (XRD) and Raman spectroscopy. As shown in Fig. S2, the NPC derived from the direct pyrolysis of indole-HCP precursors exhibits two peaks at 26.2^0 and 42.9^0, corresponding to the graphite (002) and (101) facets, respectively.[32] Notably, the peak at 26.2^0 is relatively narrow, indicating a high degree of graphitization in the carbon skeleton. In contrast, NPC-Na, NPC-Zn, and NPC-Fe exhibit broader peaks at the two positions, suggesting the formation of an amorphous structure in the carbon framework after the salt treatment. Furthermore, the peak of NPC-Na shifts towards a lower degree, indicating an increase in the interlayer space for samples treated with sodium chloride.

Further quantitative analysis of the defect quantity in all samples is conducted using Raman spectroscopy. The spectra can be fitted into four different bands by Gaussian simulation, namely D_2 (1200 cm^{-1}), D_1 (1350 cm^{-1}), D_3 (1500 cm^{-1}), and G (1587 cm^{-1}).[33] The D_1 band corresponds to the vibrational mode with A_{1g} symmetry of carbon atoms at the edges of graphene sheets. In contrast, the D_2 band is associated with carbon atoms outside the perfectly planar structure of graphene. Furthermore, the D_3 band is attributed to carbon atoms in various configurations, such as bonding with heteroatoms, forming pentagonal structures, or presenting in amorphous carbon form.[34] The defective degrees in the samples are typically represented by the I_{D1}/I_G ratio.[33, 35, 36] The

calculated results indicate that the I_{D1}/I_G value for NPC is 1.27 (Fig. 2a). In comparison, molten-salt assisted pyrolysis significantly increases the defect degree in the samples, with NPC-Na, NPC-Zn, and NPC-Fe showing values of 1.63, 1.54, and 1.45, respectively. This suggests that the highest defect extent is achieved in samples treated with sodium chloride.

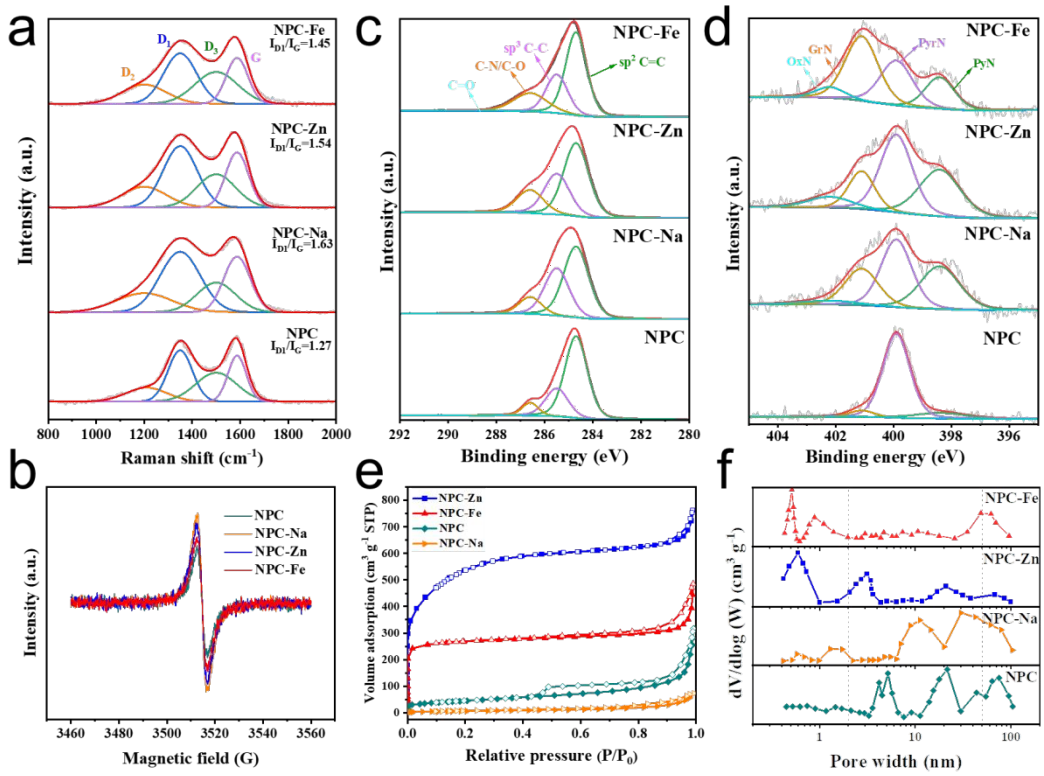

Figure 2. Physiochemical structure analysis of NPC samples. (a) Raman spectra; (b) EPR spectra; (c) high-resolution C 1s XPS spectra; (d) high-resolution N 1s XPS spectra; (e) nitrogen adsorption-desorption isotherms and (f) corresponding pore size distribution curves of NPC, NPC-Na, NPC-Zn and NPC-Fe.

For the evolution of the D_2 and D_3 bands (Table S1), it is observed that the NPC sample exhibits a D_2 peak area percentage of 17.5% and a D_3 area percentage of 32.8%.

In contrast, the samples treated with sodium chloride (NPC-Na), zinc chloride (NPC-Zn), and iron chloride (NPC-Fe) display D_2 area percentages of 17.6%, 18.2%, and 25.6%, respectively, while their D_3 area percentages are 18.5%, 24.1%, and 23.9%, respectively. These results demonstrate that the presence of molten salts during sample preparation significantly affects the D_2 and D_3 peaks. Specifically, the D_2 peak area increases moderately with the use of zinc chloride and iron chloride, indicating an increase in structural irregularities. However, the D_3 peak area shows a notable decrease in all samples treated with molten salts compared to the NPC sample. The D_3 peak areas for NPC-Na (18.5%), NPC-Zn (24.1%), and NPC-Fe (23.9%) are significantly lower than 32.8% for the NPC sample. This suggests that the introduction of molten salts during sample preparation may facilitate the partial transformation of pentagon defects, reducing the overall disorder or defectiveness associated with these configurations. Additionally, the observed changes in D_3 peak areas correlate with the heteroatom content in the samples: 4.35% of NPC-Fe, 5.31% of NPC-Zn, and 5.22% of NPC-Na (Table S2). The change trend in D_3 peak area aligns with the variation in heteroatom content, indicating that molten salt treatments contribute to structural changes in the carbon network, potentially through mechanisms involving heteroatom integration and defect transformation.

Additionally, electron paramagnetic resonance (EPR) patterns (Fig. 2b) are consistent with the Raman analysis, where the higher peak intensities are observed for NPC-Na, NPC-Zn, and NPC-Fe at the magnetic field of 3512.24 G in comparison with that of NPC, further underscoring the significant role of the molten-salt assisted method

in increasing defective sites in carbon materials [34]. Furthermore, the defect degree is also analyzed using the ratio of sp^3-C to sp^2-C. High-resolution C 1s X-ray photoelectron spectroscopy (XPS) spectra deconvolution (Fig. 2c) reveals that NPC-Na exhibits the highest sp^3-C to sp^2-C ratio of 0.65 (Table S3). In comparison, NPC-Zn and NPC-Fe display lower ratios of 0.57 and 0.48, respectively, and the NPC sample, which is directly thermalized from indole-HCP without molten salt treatment, shows the lowest ratio of 0.35. This trend correlates well with the results obtained from Raman results, demonstrating that the molten salt-assisted method indeed enhances the defect structure in indole-HPC-derived carbon materials.

Following the analysis of defect structures as one of the active sites in electrocatalytic ORR, another type of active site, namely the nitrogen dopant, is also examined. The N 1s XPS spectra of all the samples are deconvoluted into four peaks (Fig. 2d), corresponding to pyridinic nitrogen (PyN) at 398.4 eV, pyrrolic nitrogen (PyrN) at 399.9 eV, graphitic nitrogen (GrN) at 401.1 eV, and oxidized nitrogen (OxN) at 402.2 eV.[37] For the NPC sample, PyrN predominates with 81.68% ratio. Interestingly, samples treated with molten salt exhibit a higher proportion of PyN and GrN, which have been shown to enhance electrocatalytic ORR performance significantly.[38, 39] This could be attributed to atomic rearrangement and structural transformation of the indole-HCP precursor during molten salt-assisted pyrolysis. Notably, NPC-Na, NPC-Zn, and NPC-Fe all exhibit similar PyN+GrN contents around 50% (details can be seen in Table S4), significantly exceeding the 16.48% in NPC. Therefore, it can be inferred from N 1s XPS analysis that the molten salt-assisted method can modulate the configuration of

nitrogen active sites in indole-HCP, thereby impacting its ORR performance.

The pore structure and SSA can, to some extent, determine the charge transfer pathway and affect the utilization efficiency of the active sites inherent in the material. As a result, nitrogen adsorption-desorption tests (Fig. 2e) are conducted to calculate the SSA. The Brunauer-Emmett-Teller (BET) SSA of NPC samples is determined to be 161.13 m^2 g^{-1}. However, the SSA of samples treated with molten salt varies significantly (Table S3). Specifically, NPC-Zn exhibits the highest SSA of 1912.29 m^2 g^{-1}, primarily due to the generation of a large number of micropores during the thermal treatment of carbon materials with zinc chloride.[40] This could be validated by its quasi-Type-I isotherm and the pore size distribution (PSD, Fig. 2f). Surprisingly, NPC-Na shows the lowest SSA of 23.26 m^2 g^{-1}, possibly due to the collapse of microporous structures during the thermal treatment process with sodium chloride, as evidenced in the PSD results. NPC-Fe possesses a SSA of 900.80 m^2 g^{-1}, which is intermediate between the NPC-Na and NPC-Zn. Nitrogen adsorption-desorption test results indicate that molten salt-assisted pyrolysis can significantly alter the SSA and pore structure of indole-HCP precursor-derived carbon materials. Considering the similar quantities of both defect structures and nitrogen active sites in all samples, this offers substantial potential advantages for studying the utilization efficiency of active sites via this material system. However, the SSA and pore structure determined by nitrogen adsorption-desorption analysis alone cannot fully reflect the utilization of active sites under the real electrochemical process, as some pores may not function in the actual reaction conditions.[38, 41]

To better assess the effective surface area of materials in the electrocatalytic ORR process, the double-layer capacitance (C_{dl}) of this series of samples is tested in the non-Faradaic region (Fig. S3-6), and the electrochemical active surface area (ECSA) is calculated (details can be seen in Table S3). The results show that NPC-Zn still possesses the highest ECSA of 1249.4 $m^2 g^{-1}$, while NPC-Na has the lowest of 91.9 $m^2 g^{-1}$. This further confirms from the electrochemical perspective that the samples treated with zinc chloride hold a larger active area suitable for electrochemical reactions, ensuring maximal utilization of their active sites.

Benefiting from the abundance of active sites within the material system, the carbon materials derived from indole-HCP precursors hold promise as catalysts for the electrocatalytic ORR process. Initially, their activity is assessed using the cyclic voltammetry (CV) method. In the oxygen-saturated 0.1 M KOH aqueous solution, all samples exhibit a distinct oxygen reduction peak (Fig. 3a), which is absent in the nitrogen-saturated one. NPC-Zn demonstrates the most positive oxygen reduction potential at 0.86 V vs. RHE, indicating its highest ORR activity. Linear sweep voltammetry (LSV) polarization curves (Fig. 3b) reveal that NPC-Zn exhibits the best ORR activity, which is specifically evidenced by its highest half-wave potential ($E_{1/2}$) of 0.859 V vs. RHE and a kinetic current density (J_k) of 102.64 mA cm^{-2} at 0.6 V vs. RHE. The catalytic performance of NPC-Zn is even comparable to that of the commercial Pt/C (20 wt%) catalyst with a $E_{1/2}$ of 0.862 V vs. RHE and a J_k of 108.38 mA cm^{-2} (Fig. 3c). Notably, the NPC-Na sample, which possesses the richest defect structure, exhibits the lowest ORR performance, with a $E_{1/2}$ of only 0.693 V vs. RHE

and a J_k of 27.89 mA cm^{-2}, even lower than that of NPC. This result is totally different from the traditional view that a higher number of active sites leads to increased activity.[20] Therefore, further research is required to understand the structure-property relationship of carbocatalysts in the ORR process, which will be discussed in detail in the following part of this study.

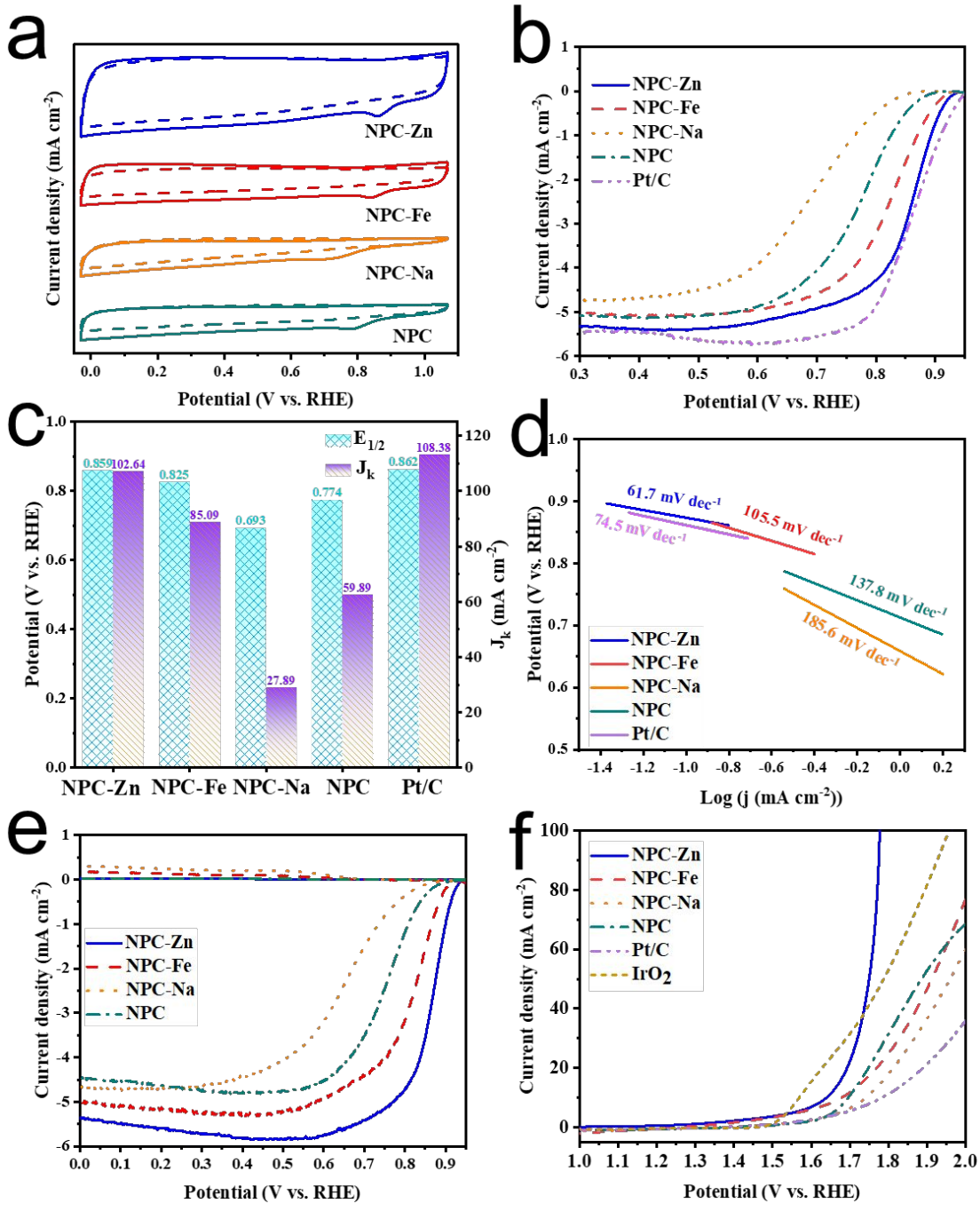

Figure 3. Electrochemical analysis of the ORR and OER performance for NPC, NPC-

Na, NPC-Zn and NPC-Fe. (a) CV curves tested in 0.1 M KOH solution saturated with nitrogen (dash line)/ oxygen (solid line); (b) LSV curves tested on RDE at 1600 rpm saturated with oxygen; (c) comparison of the $E_{1/2}$ and J_k obtained at 0.6 V vs. RHE; (d) Tafel plots; (e) LSV curves tested on RRDE at 1600 rpm saturated with oxygen; (f) LSV curves tested on RDE at 1600 rpm saturated with oxygen.

Tafel plots are subsequently adopted to investigate the kinetics of the ORR process. The NPC-Zn sample shows the lowest Tafel slope of 61.7 mV dec^{-1} (Fig. 3d), suggesting the smoothest ORR kinetics among the samples. In contrast, NPC-Na exhibits the highest Tafel slope of 185.6 mV dec^{-1}, indicating even slower reaction kinetics than the NPC sample. To further monitor electron transfer number during the reaction, LSV curves using a rotating disk electrode (RDE) are tested (Fig. S7-10), and the electron transfer number is calculated in conjunction with the Koutecký-Levich (K-L) plots within the experimental voltage range. The results show that between 0.35-0.55 V vs. RHE, the electron transfer number for NPC-Zn ranges from 3.93 to 3.96 (Fig. S11), significantly higher than other molten salt-treated samples and the NPC sample. Additionally, ring currents are collected (Fig. 3e) using a rotating ring-disk electrode (RRDE) to monitor the electron transfer number and H_2O_2 yields. Within a broad potential range of 0-0.8 V vs. RHE, the electron transfer number for NPC-Zn consistently remains between 3.90 and 3.98, while the corresponding H_2O_2 yield is lower than 5% (Fig. S12), demonstrating its excellent four-electron transfer pathway for ORR. In contrast, NPC-Fe and NPC exhibit relatively lower electron transfer

numbers and higher hydrogen peroxide yields. The electron transfer number of NPC-Na is even below 3.60 in the range of 0-0.5 V vs. RHE, with a high H_2O_2 yield reaching nearly 20%, indicating partial two-electron processes during its ORR catalysis.

Furthermore, methanol-poisoning resistance and long-term stability are important criteria for ORR catalysts in zinc-air battery (ZAB) cathodes. NPC-Zn exhibits exceptional methanol-poisoning resistance (Fig. S13a), and the addition of methanol results in virtually no decay in current over the subsequent 1600 seconds, markedly outperforming the Pt/C catalyst. A chronoamperometric test conducted over 16,000 seconds shows that NPC-Zn maintains 91.7% of its initial current value (Fig. S13b), while the decay is much more significant for the Pt/C catalyst. These results suggest that NPC-Zn holds tremendous advantages as an ORR catalyst.

To demonstrate the reliability of the samples as bifunctional catalysts in rechargeable ZAB, oxygen evolution reaction (OER) performance is measured in the 0.1 M KOH aqueous solution. The NPC-Zn sample exhibits the lowest overpotential of 410 mV at 10 mA cm^{-2}, comparable to the 339 mV of the commercial benchmark IrO_2 catalyst (Fig. 3f). In contrast, the overpotentials for NPC-Fe, NPC-Na, and NPC are 453, 513, and 466 mV, respectively, indicating that NPC-Zn is more favorable for facilitating the OER process. This is probably attributed to the maximized utilization of its rich defect structures and nitrogen-doped active sites within the high ECSA. A comparison of Tafel slopes (Fig. S14) reveals that NPC-Zn has a significantly lower slope of 71.8 mV dec^{-1} compared to the other samples, which is even lower than the 74.5 mV dec^{-1} of IrO_2, indicating its superior OER reaction kinetics.

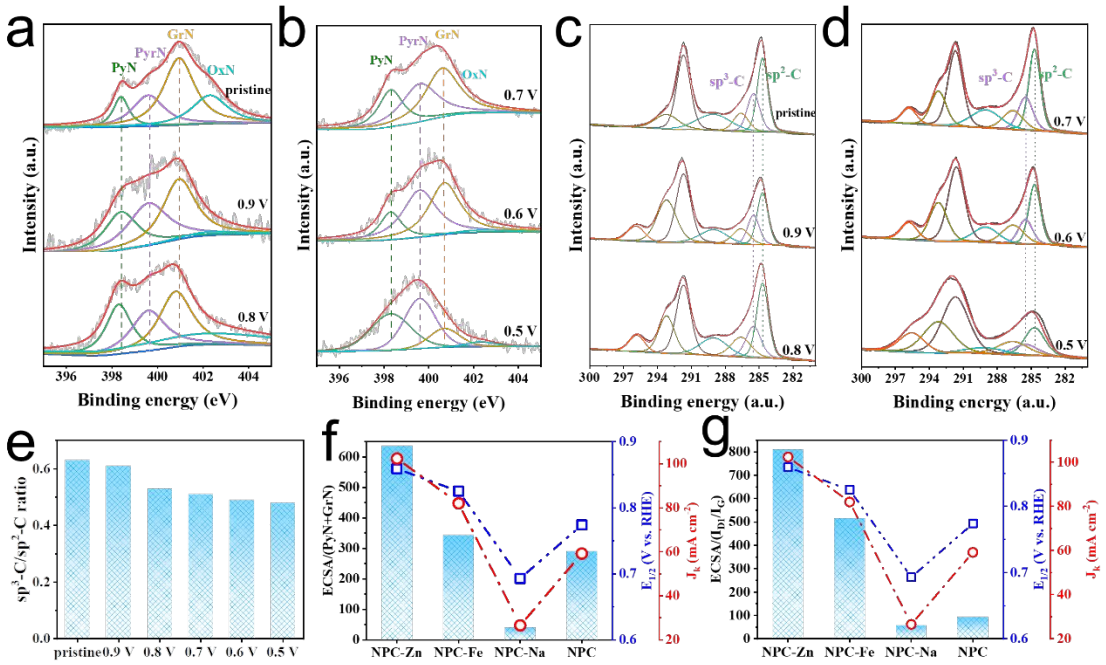

Figure 4. Mechanism analysis and the construction of structure-property relationship. (a)-(b) Ex-situ XPS N 1s spectra and (c)-(d) ex-situ XPS C 1s spectra of NPC-Zn during the LSV measurement; (e) the variation of sp^3-C/sp^2-C ratio along with the overpotential increases; (f) the relationship constructed between ECSA/(PyN+GrN) and $E_{1/2}$ as well as J_k; (g) the relationship constructed between ECSA/(I_D+I_G) and $E_{1/2}$ as well as J_k.

To elucidate the role of maximizing the utilization for active sites in enhancing ORR performance, we further focus on the identification of active sites and the establishment of structure-property relationship. Ex-situ XPS analysis is conducted to deconvolute the N 1s XPS and C 1s XPS spectra of NPC-Zn at different potentials. Analysis of changes in the N 1s XPS spectra (Fig. 4a-b) reveals that as the overpotential gradually increases to 0.8 V vs. RHE, notable shifts occur in the positions of PyN and GrN, while the

position of PyrN remains unchanged. Furthermore, as the overpotential increases to 0.5 V vs. RHE, the peak areas of PyN+GrN significantly decrease, indicating that PyN and GrN serve as the main active nitrogen-doped sites during the ORR process. On the other hand, the changes observed in the C 1s XPS spectra (Fig. 4c-d) show a continuous decrease in the sp^3-C/sp^2-C content with increasing overpotential (Fig. 4e), suggesting that defect structures indeed participate in the ORR process and interact strongly with intermediate species (such as O_2* or *OOH) [42]. In sum, ex-situ XPS analysis clearly identifies the main active sites in the NPC-Zn material system during the electrocatalytic ORR process, including the nitrogen species of PyN and GrN, as well as defect structures.

To ascertain the extent of maximization of active site utilization in NPC-Zn, two parameters are extracted: ECSA/[PyN+GrN] and ECSA/[I_{D1}/I_G]. These parameters can be interpreted, from a physical perspective, as the active surface area available per unit of active site, termed EPA. Evidently, for a given number of active sites, a higher ECSA value implies a fuller utilization, thereby leading to superior ORR performance. Accordingly, we establish structure-property relationships correlating these parameters (EPA) with $E_{1/2}$, a performance parameter representing ORR activity, and J_k, a parameter indicating kinetic performance. The results show strong consistency between the structure and the performance parameters, indicating that NPC-Zn, with the highest ECSA/[PyN+GrN] and ECSA/[I_{D1}/I_G] ratios, exhibits higher $E_{1/2}$ and J_k (Fig. 4f-g). For NPC-Na, despite its substantial number of active sites, including PyN+GrN and I_{D1}/I_G ratios, its low ECSA restricts the full utilization of these sites, thereby diminishing its

ORR performance. In contrast, NPC, albeit having a lower number of active sites, demonstrates certain ORR performance due to its relatively higher ECSA. This indicates that for carbocatalysts in ORR processes, the key to fully leveraging active sites lies in enhancing the ECSA.

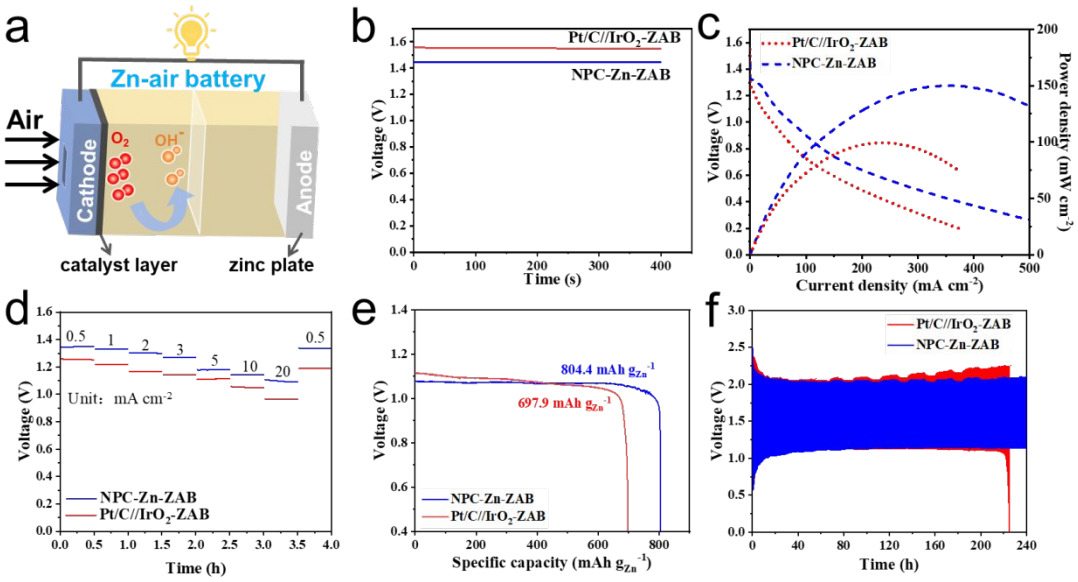

Figure 5. ZAB performance of NPC-Zn-ZAB and Pt/C//IrO_2-ZAB. (a) Schematic illustration of the NPC-Zn-ZAB; (b) OCV curves; (c) polarization and power density curves; (d) rate capability; (e) discharge specific capacity; (f) galvanostatic charge/discharge cycling curves at 5 mA cm^{-2}.

Inspired by the excellent bifunctional ORR and OER performance, the NPC-Zn sample is utilized as the cathode catalyst to assemble a rechargeable zinc-air battery, designated NPC-Zn-ZAB (Fig. 5a). Compared to the ZAB assembled using commercial Pt/C and IrO_2 catalysts (designated Pt/C//IrO_2-ZAB), the open-circuit voltage (OCV) of NPC-Zn-ZAB is 1.443 V (Fig. 5b), closely approaching the 1.554 V of Pt/C//IrO_2-ZAB. The discharge polarization curve (Fig. 5c) results indicate that the peak power

density of NPC-Zn-ZAB reaches 149.6 mW cm^{-2}, even surpassing 99.2 mW cm^{-2} of Pt/C//IrO_2-ZAB, demonstrating superior discharge performance of NPC-Zn-ZAB. Rate capability test (Fig. 5d) reveals that the output voltage of NPC-Zn-ZAB at different current densities exceeds that of Pt/C//IrO_2-ZAB, and when the discharge current density is restored to 0.5 mA cm^{-2}, its output voltage recovers to the initial 1.37 V, indicating ideal rate capability and reversibility of NPC-Zn as the cathode for ZAB.

Furthermore, based on the mass of consumed zinc metal, the discharge specific capacity (Fig. 5e) is calculated and reveals that NPC-Zn-ZAB could exhibit a specific capacity of 804.4 mAh g^{-1}, surpassing the 697.9 mAh g^{-1} of Pt/C//IrO_2-ZAB, which indicates excellent energy storage performance for the former. Finally, the cycling stability of ZAB is tested at a current density of 5 mA cm^{-2}(Fig. 5f). NPC-Zn-ZAB exhibits a smaller overvoltage gap and remains very stable after working for 240 hours, whereas Pt/C//IrO_2-ZAB shows a significant increase in the overpotential gap after 120 hours and a drastic deterioration after 220 hours, further evidencing the excellent reversibility of NPC-Zn-ZAB. Moreover, the average Coulombic efficiency (CE) for NPC-Zn-ZAB after 240 hours is 71.4% (Fig. S15a), which is notably higher than the 70.1% observed for Pt/C//IrO_2-ZAB (Fig. S15b). This indicates a substantial improvement in energy conversion efficiency, demonstrating the superior performance and stability of NPC-Zn as a promising candidate for high-efficiency zinc-air batteries.

Finally, we transform the excellent carbocatalyst suitable for ORR into an electrode material for a capacitive deionization (CDI) device (designated NPC-Zn-CDI), and further power this NPC-Zn-CDI with NPC-Zn-ZAB to optimize energy utilization and

efficiently address environmental pollution, achieving a purpose of killing two birds with one stone. This strategy is inspired by the following three factors: (i) Considering that NPC-Zn exhibits exceptional SSA and ECSA, we hypothesize that NPC-Zn holds significant potential in charge storage, capable of effectively adsorbing and desorbing sodium and chloride ions in CDI applications. (ii) The driving voltage for CDI devices typically revolves around 1.4 V, while the open-circuit voltage of NPC-Zn-ZAB is 1.443 V, suggesting the feasibility of powering the NPC-Zn-CDI with NPC-Zn-ZAB. (iii) NPC-Zn-ZAB possesses a high energy density, attributable to one of its reactive substances, oxygen, which diffuses from the air through the gas diffusion layer (GDL) to the electrode surface to participate in the reaction. Concurrently, NPC-Zn-CDI effectively reduces the high salt concentration in wastewater. By coupling the high-energy-density NPC-Zn-ZAB with the environmentally friendly NPC-Zn-CDI device, this integration could facilitate efficient resource management of energy and the environment.

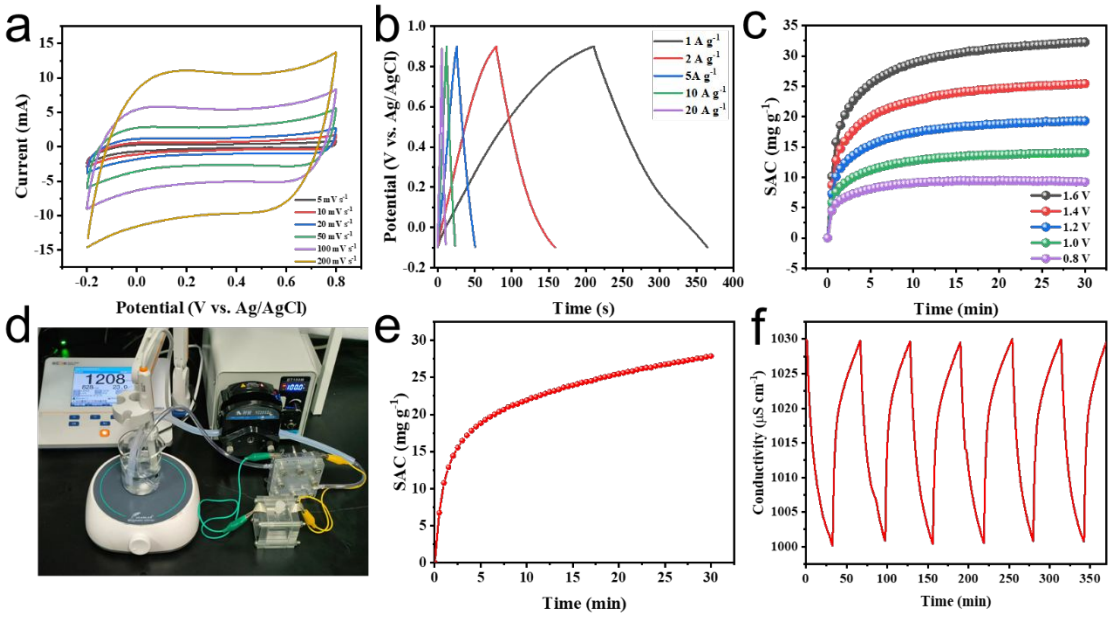

Figure 6. Application of NPC-Zn-ZAB as the power for driving an NPC-Zn-based CDI

device. (a) CV curves of the NPC-Zn electrode in 1.0 M NaCl solution over a potential range from -0.2 to 0.8 V at different scan rates; (b) galvanostatic charge-discharge curves at different current densities; (c) plots of salt adsorption capacity (SAC) vs. desalination time at different voltages; (d) photograph of NPC-Zn-based CDI setup powered by NPC-Zn-ZAB; (e) the SAC curve and (f) CDI cycling performance of NPC-Zn powered by NPC-Zn-ZAB.

The CDI performance of the NPC-Zn electrode was evaluated by CV and galvanostatic charge/discharge (GCD) analysis in a three-electrode system using 1.0 M NaCl solution as the electrolyte. The CV curves (Fig. 6a) of NPC-Zn exhibit a quasi-rectangular shape, suggesting a typical double layer capacitance (EDLC) behavior during the charge/ discharge process, which could be corroborated by the GCD plots with a symmetric triangular pattern (Fig. 6b). Notably, NPC-Zn exhibits a high specific capacitance of 211.3 F g^{-1} at 1 A g^{-1}, and could retain 104.0 F g^{-1} even at a high current density of 20 A g^{-1}, indicating the NPC-Zn sample holds great promise as an electrode in CDI desalination. The CDI cell is assembled using a pair of NPC-Zn electrodes of the same mass and 500 mg L^{-1} NaCl solution. As the operative voltage increases from 0.8 V to 1.6 V, the salt adsorption capacity (SAC) is also improved from 9.51 mg g^{-1} to 32.58 mg g^{-1} (Fig. 6c), outperforming the CDI performance of other carbonaceous electrodes, including NP-HPCN-900 [43] (18.1 mg g^{-1} at 1.4 V), HCNSs [44] (18.04 mg g^{-1} at 1.2 V) and PPD-CNTs@MC [45] (15.6 mg g^{-1} at 1.2 V). Accordingly, the direct-current supply is replaced by the NPC-Zn-ZAB to power the NPC-Zn-based CDI device (Fig.

6d). Impressively, a high SAC of 27.8 mg g^{-1} could be maintained (Fig. 6e), surpassing the value of 25.4 mg g^{-1} at 1.4 V driven by the direct-current supply operated under the same conditions. Moreover, after 6 hours of adsorption-desorption cycling (Fig. 6f), the desalination capability could still be retained, demonstrating the excellent stability of the NPC-Zn-based CDI which is powered by the NPC-Zn-ZAB. These encouraging results imply that NPC-Zn-ZAB could serve as a stable power source, providing an alternative for electricity supply in specific scenarios.

4. Conclusion

In summary, we have demonstrated a novel approach through the molten salt-regulated synthesis of indole-based porous polymers, leading to the development of nitrogen-doped porous carbon materials (NPC) with customizable active site quantities and specific surface areas. This strategy directly addresses the challenge of active site underutilization in carbon nanomaterials for electrocatalytic ORR. The systematic analysis reveals a significant correlation between the microenvironment of the active sites, particularly the electrochemical active surface area (ECSA), and ORR performance. Significantly, the ECSA per active site (EPA) is identified as a pivotal determinant, with the NPC-Zn catalyst showcasing superior performance metrics, including an impressive half-wave potential of 0.859 V vs. RHE and kinetic current density of 102.64 mA cm^{-2}. The application of NPC-Zn in rechargeable zinc-air batteries (ZAB) delivers a high open circuit voltage of 1.443 V and a power density of 149.6 mW cm^{-2}, while its use in capacitive deionization (CDI) devices achieves a remarkable salt adsorption capacity of 32.58 mg g^{-1}. Notably, the NPC-Zn-ZAB could

alternatively power the NPC-Zn-based CDI, achieving a high SAC of 27.8 mg g^{-1}, comparable to that powered by a direct-current supply. Our findings not only pave the way for enhancing active site utilization efficiency in carbocatalysts but also provide valuable insights for the rational design of high-performance ORR electrocatalysts. In addition, this work also holds significant promise for advancing environmental energy technologies, with broad implications for the development of sustainable energy solutions.

Acknowledgement

The authors acknowledge the financial support from the Science Research Project of the Hebei Education Department (BJK2023021), the National Natural Science Foundation of China (U20A20131 and 22005084), the Basic Research Project of Shijiazhuang Municipal Universities in Hebei Province (241790647A), the Natural Science Foundation of Hebei Province (E2019204131, B2024204010), the Central Government Guided Local Science and Technology Development Fund Projects (236Z3601G), and the UQ-Yonsei International Project. We express our gratitude to the English editing software, such as Grammarly and ChatGPT, for refining the language and checking grammatical errors in our manuscript. Additionally, this work utilized the Queensland node of the NCRIS-enabled Australian National Fabrication Facility (ANFF).

Conflict of interest

The authors declare that they have no conflict of interest.

References

1 W. Sun, F. Wang, B. Zhang, M. Zhang, V. Kuepers, X. Ji, C. Theile, P. Bieker, K. Xu, C. Wang and M. Winter, *Science*, 2021, **371**, 46-51.

2 J. Fu, R. Liang, G. Liu, A. Yu, Z. Bai, L. Yang and Z. Chen, *Adv. Mater.*, 2019, **31**, 1805230.

3 J. Zhang, Z. Zhao, Z. Xia and L. Dai, *Nat. Nanotechnol.*, 2015, **10**, 444-452.

4 Z. W. Seh, J. Kibsgaard, C. F. Dickens, I. B. Chorkendorff, J. K. Norskov and T. F. Jaramillo, *Science*, 2017, **355**, eaad4998.

5 X. Zou, M. Tang, Q. Lu, Y. Wang, Z. Shao and L. An, *Energy Environ. Sci.*, 2024, **17**, 386-424.

6 S. Zago, L. C. Scarpetta-Pizo, J. H. Zagal and S. Specchia, *Electrochem. Energy Rev.*, 2024, **7**, 1.

7 M. Du, D. Li, S. Liu and J. Yan, *Adv. Funct. Mater.*, 2023, **33**, 202301527.

8 Y. Jia and X. Yao, *Acc. Chem. Res.*, 2023, **56**, 948-958.

9 K. Gong, F. Du, Z. Xia, M. Durstock and L. Dai, *Science*, 2009, **323**, 760-764.

10 W. Ding, Z. Wei, S. Chen, X. Qi, T. Yang, J. Hu, D. Wang, L. J. Wan, S. F. Alvi and L. Li, *Angew. Chem. Int. Ed.*, 2013, **52**, 11755-11759.

11 L. Lai, J. R. Potts, D. Zhan, L. Wang, C. K. Poh, C. Tang, H. Gong, Z. Shen, J. Lin and R. S. Ruoff, *Energy Environ. Sci.*, 2012, **5**, 7936.

12 D. Guo, R. Shibuya, C. Akiba, S. Saji, T. Kondo and J. Nakamura, *Science*, 2016, **351**, 361-365.

13 J. J. Wu, L. L. Ma, R. M. Yadav, Y. C. Yang, X. Zhang, R. Vajtai, J. Lou and

P. M. Ajayan, *ACS Appl. Mater. Inter.*, 2015, **7**, 14763-14769.

14 H. Yu, L. Shang, T. Bian, R. Shi, G. I. N. Waterhouse, Y. Zhao, C. Zhou, L.-Z. Wu, C.-H. Tung and T. Zhang, *Adv. Mater.*, 2016, **28**, 5080-5086.

15 D. Li, Y. Jia, G. Chang, J. Chen, H. Liu, J. Wang, Y. Hu, Y. Xia, D. Yang and X. Yao, *Chem*, 2018, **4**, 2345-2356.

16 Y. Jia, L. Zhang, L. Zhuang, H. Liu, X. Yan, X. Wang, J. Liu, J. Wang, Y. Zheng, Z. Xiao, E. Taran, J. Chen, D. Yang, Z. Zhu, S. Wang, L. Dai and X. Yao, *Nat. Catal.*, 2019, **2**, 688-695.

17 J. Zhang, Y. Sun, J. Zhu, Z. Gao, S. Li, S. Mu and Y. Huang, *Adv. Sci.*, 2018, **5**, 1801375.

18 Y. Bian, H. Wang, J. Hu, B. Liu, D. Liu and L. Dai, *Carbon*, 2020, **162**, 66-73.

19 S. N. Stamatin, I. Hussainova, R. Ivanov and P. E. Colavita, *ACS Catal.*, 2016, **6**, 5215-5221.

20 Q. Wu, Y. Jia, Q. Liu, X. Mao, Q. Guo, X. Yan, J. Zhao, F. Liu, A. Du and X. Yao, *Chem*, 2022, **8**, 2715-2733.

21 Z. Xiao, X. Mou, X. Meng, Q. Yang, Y. Ma, N. Zhao, X. Huang, U. Shaislamov, D. Kong and L. Zhi, *Appl. Surf. Sci.*, 2022, **599**, 153961.

22 Y. Ding, W. Zhou, J. Li, J. Wang, L. Xie, X. Meng, J. Gao, F. Sun, G. Zhao and Y. Qin, *ACS Energy Lett.*, 2023, **8**, 3122-3130.

23 Lingyan Jing, Qiang Tian, Wenyi Wang, Xuan Li, Qi Hu, Hengpan Yang and C. He, *Adv. Energy Mater.*, 2024, DOI: 10.1002/aenm.202304418, 2304418.

24 H. Meng, B. Wu, D. Zhang, X. Zhu, S. Luo, Y. You, K. Chen, J. Long, J. Zhu,

L. Liu, S. Xi, T. Petit, D. Wang, X.-M. Zhang, Z. J. Xu and L. Mai, *Energy Environ. Sci.*, 2024, **17**, 704-716.

25 S. K. Kaiser, Z. Chen, D. Faust Akl, S. Mitchell and J. Perez-Ramirez, *Chem. Rev.*, 2020, **120**, 11703-11809.

26 S. Ye, V. Lotocki, H. Xu and D. S. Seferos, *Chem. Soc. Rev.*, 2022, **51**, 6442-6474.

27 Y. Gu, S. U. Son, T. Li and B. Tan, *Adv. Funct. Mater.*, 2020, **31**, 2008265.

28 Z. Xiao, D. Kong, J. Liang, B. Wang, R. Iqbal, Q.-H. Yang and L. Zhi, *Carbon*, 2017, **116**, 633-639.

29 Y. Yang, Y. P. Ma, C. C. Lu, S. J. Li and M. Y. Zhu, *Green Chem.*, 2023, **25**, 10209-10234.

30 C. J. Xuan, B. S. Hou, W. W. Xia, Z. K. Peng, T. Shen, H. L. Xin, G. A. Zhang and D. L. Wang, *J. Mater. Chem. A*, 2018, **6**, 10731-10739.

31 X.-Y. Xin, B. Zhao, J.-S. Yue, D.-B. Kong, S.-K. Zhou, X.-X. Huang, B. Wang, L.-J. Zhi and Z.-C. Xiao, *New Carbon Mater.*, 2023, **38**, 898-912.

32 C. Zhang, W. Shen, K. Guo, M. Xiong, J. Zhang and X. Lu, *J. Am. Chem. Soc.*, 2023, **145**, 11589-11598.

33 G. Ye, S. Liu, K. Huang, S. Wang, K. Zhao, W. Zhu, Y. Su, J. Wang and Z. He, *Adv. Funct. Mater.*, 2022, **32**, 2111396.

34 N. Li, K. Guo, M. Li, X. Shao, Z. Du, L. Bao, Z. Yu and X. Lu, *J. Am. Chem. Soc.*, 2023, **145**, 24580-24589.

35 Q. Wang, F. Liu, Z. Jin, X. Qiao, H. Huang, X. Chu, D. Xiong, H. Zhang, Y.

Liu and W. Yang, *Adv. Funct. Mater.*, 2020, **30**, 2002580.

36 Y. J. Sa, J. H. Kim and S. H. Joo, *Angew. Chem. Int. Ed.*, 2019, **58**, 1100-1105.

37 H. Xia, R. Pang, X. Dong, Q. Liu, J. Chen, E. Wang and J. Li, *J. Am. Chem. Soc.*, 2023, **145**, 25695-25704.

38 Y. Pan, Y. Xin, Y. Li, Z. Xu, C. Tang, X. Liu, Y. Yin, J. Zhang, F. Xu, C. Li and Y. Mai, *ACS Nano*, 2023, **17**, 23850-23860.

39 B. Wu, H. Meng, D. M. Morales, F. Zeng, J. Zhu, B. Wang, M. Risch, Z. J. Xu and T. Petit, *Adv. Funct. Mater.*, 2022, DOI: 10.1002/adfm.202204137, 2204137.

40 L. Jiaxu, X. Zhichang, G. Yang, X. Xiaohui, K. Debin, W. Manfred and Z. Linjie, *Carbon*, 2019, **143**, 487-493.

41 X. Wang, T. Liu, H. Li, C. Han, P. Su, N. Ta, S. P. Jiang, B. Kong, J. Liu and Z. Huang, *Nano Lett.*, 2023, **23**, 4699-4707.

42 L. Jing, Q. Tian, X. Li, J. Sun, W. Wang, H. Yang, X. Chai, Q. Hu and C. He, *Adv. Funct. Mater.*, 2023, **33**, 202305795.

43 S. Huo, Y. Zhao, M. Zong, B. Liang, X. Zhang, I. U. Khan, X. Song and K. Li, *J. Mater. Chem. A*, 2020, **8**, 2505-2517.

44 Y. Tang, J. Ding, W. Zhou, S. Cao, F. Yang, Y. Sun, S. Zhang, H. Xue and H. Pang, *Adv. Sci.*, 2023, DOI: 10.1002/advs.202206960, e2206960.

45 Y. Lian, D. Wang, H. Guo, Z. Cao, J. Zhao and H. Zhang, *Carbon*, 2023, **204**, 50-56.

The raw TEM images and aberration-corrected TEM image are uploaded as part of the ESI. The data collected and produced for this work are available upon reasonable request from the corresponding authors.